Multi-modal vision-language model for generalizable annotation-free pathological lesions localization and clinical diagnosis

Hao Yang[1,2,3†], Hong-Yu Zhou[5†], Zhihuan Li[6], Yuanxu Gao[6], Cheng Li[1], Weijian Huang[1,2,3], Jiarun Liu[1,2,3], Hairong Zheng[1], Kang Zhang[4,6*], Shanshan Wang[1,2*]

[1]Paul C. Lauterbur Research Center for Biomedical Imaging, Shenzhen Institute of Advanced Technology, Chinese Academy of Sciences, Shenzhen, China.
[2]Peng Cheng Laboratory, Shenzhen, China.
[3]University of Chinese Academy of Sciences, Beijing, China.
[4]National Clinical Research Center for Ocular Diseases, Eye Hospital and Advanced Institute for Eye Health and Diseases, Wenzhou Medical University, Wenzhou, China.
[5]Department of Computer Science, The University of Hong Kong, Pokfulam, China.
[6]Instutite for Artificial Intelligence in Medicine and Faculty of Medicine, Macau University of Science and Technology, Macau, China.

*Corresponding author(s). E-mail(s): ss.wang@siat.ac.cn; kang.zhang@gmail.com;
†These authors contributed equally to this work.

Abstract

Defining pathologies automatically from medical images aids the understanding of the emergence and progression of diseases, and such an ability is crucial in clinical diagnostics. However, existing deep learning models heavily rely on expert annotations and lack generalization capabilities in open clinical environments. In this study, we present a generalizable vision-language pre-training model for Annotation-Free pathological lesions Localization (AFLoc). The core strength of AFLoc lies in its extensive multi-level semantic structure-based contrastive learning, which comprehensively aligns multi-granularity medical concepts from reports with abundant image features, to adapt to the diverse expressions of pathologies and unseen pathologies without the reliance on image annotations from experts. We demonstrate the proof of concept on CXR images, with extensive experimental validation across 4 distinct external datasets, encompassing 11 types of chest pathologies. The results demonstrate that AFLoc surpasses state-of-the-art methods in pathological lesions localization and disease classification, and even outperforms the human benchmark in locating 5 different pathologies. Additionally, we further verify its generalization ability by applying it to retinal fundus images. Our approach showcases AFoc versatilities and underscores its suitability for clinical diagnoses in complex clinical environments.

Keywords: Annotation-Free Deep Learning, pathological lesions localization, Vision-Language Pre-Training
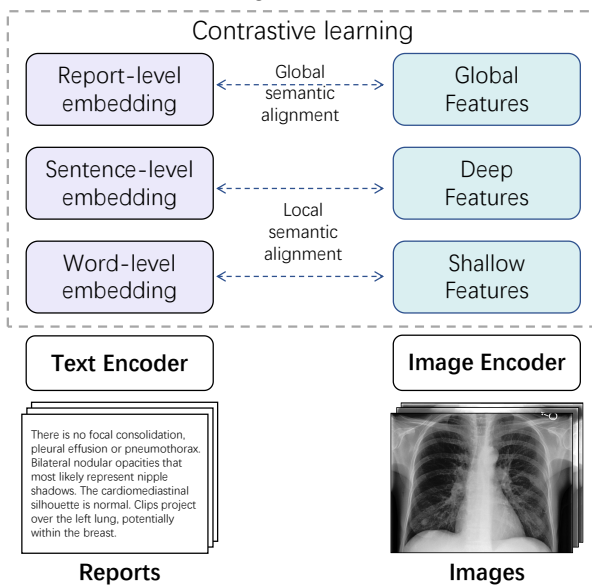
Pathological lesions localization plays a crucial role for advancing scientific research and disease diagnosis [1–4]. In the past decade, breakthrough advancements in deep learning have significantly accelerated progress within the domain of disease localization [5–8]. Nevertheless, the efficacy of these deep learning approaches is considerably constrained by their profound dependency on richly annotated training datasets [9–13]. Specifically, the annotation work required for localization tasks is particularly laborious, often involving precise bounding box or pixel-wise annotation of localized pathological areas. Compared to the image-level annotations (e.g., disease labels), the high-precision annotation efforts of localization tasks is more costly and thereby requires significantly more time investment.

The manuscript is prepared on January 20, 2024.

a. Annotation-free Vision-Language pre-training and inference pipeline
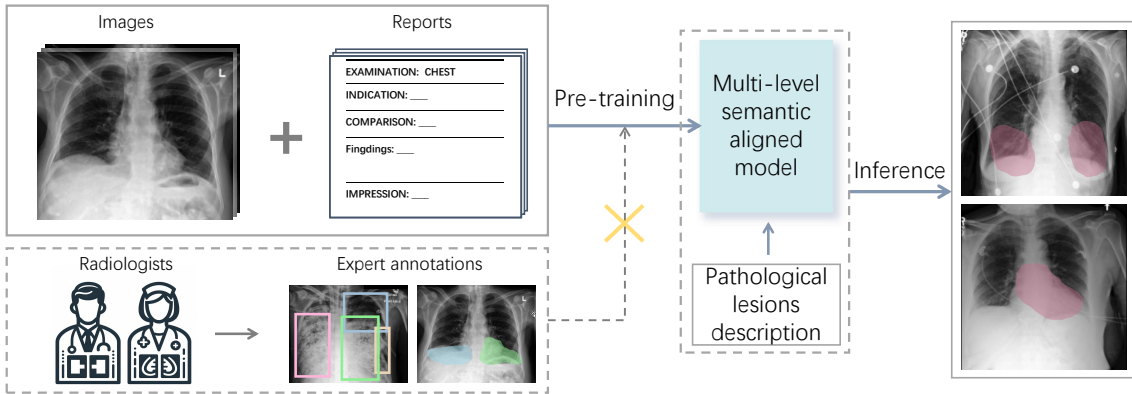
b. Multi-level semantic alignment model

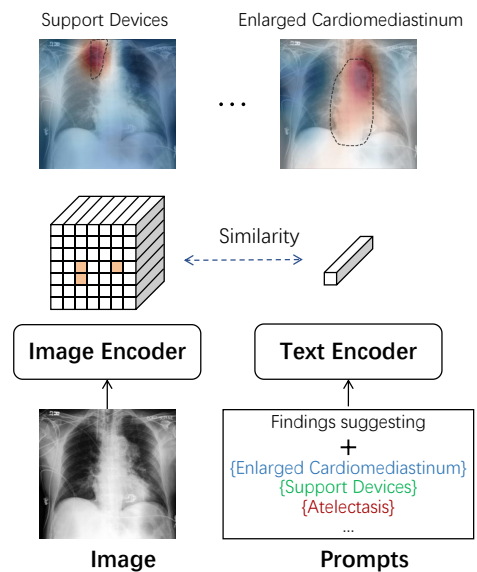**c**. Pathological lesions localization pipeline

Fig. 1: The proposed AFLoc framework. (a) Annotation-free pre-training and inference pipeline showing the system's ability to learn from unannotated images and corresponding diagnostic reports for automated inference. (b) During the pre-training stage, the image encoder and text encoder extract features of different levels from medical images and diagnostic reports, respectively, and align them through contrastive learning. (c) pathological lesions localization process, which employs pathology-related text prompts to precisely localize the pathological areas in the images.

In recent years, self-supervised pre-training [14–16] has been proposed to mitigate reliance on large annotated datasets. Initially, these methodologies acquire general visual representations via self-supervised learning from image datasets, subsequently utilizing a comparatively reduced dataset of annotated data for supervised fine-tuning of the model. This strategy enables the model to perform well on trained categories, while significantly reducing the need and cost for data labeling. Additionally, saliency methods [17–20] can also reduce the annotation costs in pathological lesions localization tasks to a certain degree because they allow for the coarse localization of target categories in models trained with image-level annotations. However, in clinical practice, models may require additional training or tuning to adapt to unseen diseases [9, 21]. This challenge is particularly acute for emerging diseases [22]. In such scenarios, rapidly acquiring a dataset with expert annotations for training or adjusting the model becomes extremely difficult. Consequently, deploying these models in an open clinical environment entails substantial challenges.

A promising solution is the development of medical vision-language pre-training models [21, 23–28]. Existing studies predominantly utilize medical images and accompanying radiology reports as foundational training data. This technique effectively diminishes the dependency on expert annotations, allowing models to directly learn from reports and absorb the biomedical domain knowledge contained therein [28]. Nevertheless, achieving

precise pathological lesions localization solely through medical images coupled with radiology reports introduces multifaceted challenges. A principal impediment in model training is the absence of definitive pathological locational markers. Specifically, despite diagnostic reports offering elaborate descriptions of disease characterizations, they often lack detailed spatial coordinates and fail to align with distinct image regions. Moreover, the variability in clinicians' descriptive methodologies may engender structural and descriptive inconsistencies in the structure and description of the reports, further complicating the task of precise disease extraction and localization in medical images.

Presently, vision-language pre-training approaches have manifested nascent progress in the domain of pathological lesions localization. The majority of studies engaged contrastive learning methodologies, directly aligning images with entire pathology reports [25, 26]. Nevertheless, these strategies often neglect fine-grained details, resulting in inaccurate localization [21]. To address this, some approaches were designed to incorporate more granular information [21, 27]. For instance, GLoRIA [27] learned global and local representations of images by comparing image sub-regions with words in the paired reports. MedKLIP [21] used a well-defined medical word knowledge base to transform medical entities into more fine-grained descriptions and provide supervision at the entity level through a triplet training paradigm. However, these fine-grained methods only focused on single-level medical concepts, neglecting the variable meanings of concepts in different contexts. For example, when a chest X-ray diagnosis report indicates opacity, the actual condition may be pulmonary edema, atelectasis, lung cancer, surgical changes, or pleural effusion [29], each requiring different contextual analysis to identify accurately, rather than relying on the opacity alone. As a result, these methods may grapple with adapting to the multifarious manifestations of disease descriptors in clinical practice, often requiring custom text prompts for enhanced localization performance [25, 27].

In this study, we present AFLoc, a vision-language pre-training model designed to alleviate the need for costly bounding boxes. AFLoc can effectively perform pathological lesions localization in chest X-ray images using brief pathologies descriptions. The overall framework of AFLoc is depicted in Fig. 1. Different from the commonly used global semantic alignment strategies [25, 26], AFLoc introduced a contrastive learning framework with a multi-level semantic alignment structure. In AFLoc, the images are processed through an encoder to generate features at three levels: shallow features, deep features, and global features. These features correspond to three different levels of embeddings extracted by the text encoder: word-level, sentence-level, and report-level. Subsequently, information from both modalities is carefully matched and aligned according to their respective granularities. The framework is capable of comprehensively aligning medical concepts from reports with image features in a shared semantic space. In the aligned semantic space, pathology can be located by matching the similarity between natural language tags/descriptions of the pathology and local images. The effectiveness of AFLoc has been validated on 4 external independent datasets, including RSNA Pneumonia [30], COVID Rural [31, 32], MS-CXR [25], and CheXlocalize [17]. The results showed that AFLoc can achieve accurate pathological lesions localization with brief descriptions for 11 types of chest pathologies and performed well in localizing unseen diseases. Moreover, this method surpasses state-of-the-art methods in disease classification capabilities. Furthermore, AFLoc's generalizability extends beyond chest X-rays to include retinal fundus images, demonstrating its potential applicability in diverse clinical scenarios. This extension to retinal fundus images showcases AFLoc's capability in handling different types of medical image, further underscoring its adaptability and efficacy in complex clinical environments.

Results

We employed chest X-ray images and radiological reports to instantiate the tasks of pathological lesions localization and disease classification without the need for training on explicit annotations. In our experiments, we initially engaged in pre-training utilizing the MIMIC-CXR dataset [33] and subsequently conducted localization evaluations across 4 external datasets, including RSNA Pneumonia [30], COVID Rural [31, 32], MS-CXR [25], and CheXlocalize [17]. Throughout the evaluation phase, the models engendered similarity maps or heatmaps (Fig. 1) through the correlation of pathology descriptors with chest X-rays. Subsequently, thresholds were meticulously applied to each similarity map, culminating in the generation of binary segmentation maps. Furthermore, we executed comprehensive ablation studies to delineate and analyze the contributions of different components of our AFLoc. For the disease classification task, we conducted additional evaluations using the RSNA Pneumonia and SIIM-ACR Pneumothorax datasets.

Two metrics were calculated to quantitatively evaluate the localization performance. Our primary metric, Intersection over Union (IoU) [34], measures the average overlap between the saliency maps generated by different methods and the ground truth segmentation maps. For RSNA Pneumonia, COVID Rural, and MS-CXR datasets, each reported IoU was averaged over multiple IoUs calculated at different threshold values, [0.1, 0.2, 0.3, 0.4, 0.5]. On the CheXlocalize dataset, to guarantee a fair comparison, we followed the methodology outlined in the reference literature [17]. An optimal threshold was ascertained from the validation set and subsequently
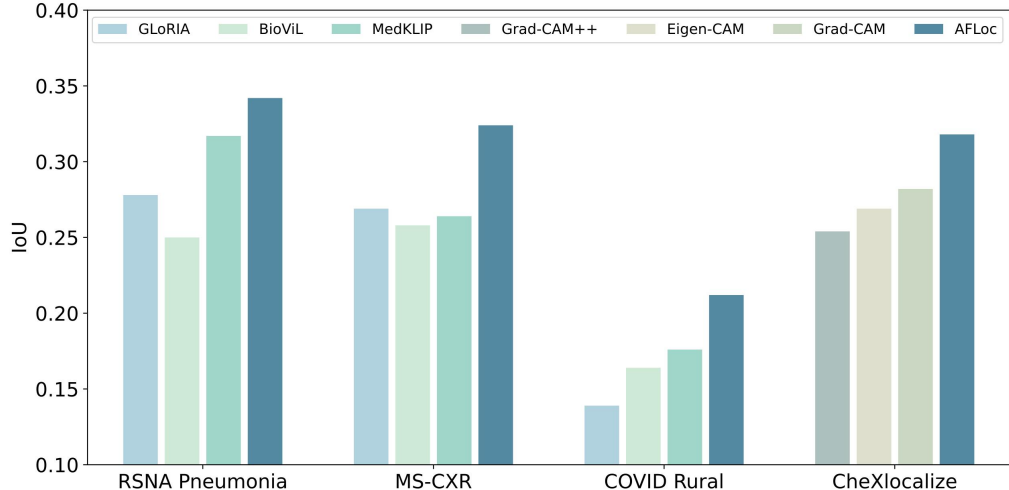
Fig. 2: Quantatitive pathological lesions localization results (IoU) of different models on the 4 datasets, RSNA Pneumonia [30], COVID Rural [31, 32], MS-CXR [25] and CheXlocalize [17]. AFLoc demonstrates consistent advantages across all evaluated datasets.

applied to the test set for comprehensive assessment. The second metric, Contrast-to-Noise ratio (CNR) [25], measures the difference between scores inside and outside the bounding box area, without the need for a hard threshold. This assessment of local similarity is significant as certain clinical downstream applications might benefit from heatmap visualizations rather than discrete segmentation masks. The averages of these metrics are reported on the test set, based on over 1,000 bootstrap repetitions, accompanied by the 95% confidence interval, which was determined using the 2.5th and 97.5th percentiles of the empirical distribution.

RSNA Pneumonia

Initially, we reported the outcomes related to pneumonia localization derived from the RSNA Pneumonia dataset. Diagnosing pneumonia accurately is a challenging task, requiring well-trained experts to review chest X-rays (CXR) and inspect various factors such as clinical history, vital signs, and laboratory exams. Pneumonia typically presents as one or multiple regions of increased opacity in CXR [29]. However, diagnosing pneumonia based on CXR can be complicated due to the presence of many other lung conditions, such as pulmonary edema, bleeding, atelectasis, lung cancer, or surgical changes. Additionally, outside the lungs, pleural effusion can also appear as increased opacity in CXR. In this context, developing automated methods for pneumonia localization can be highly beneficial in the clinical environment.

We conducted a comparative analysis of the pneumonia localization performance of our proposed AFLoc model against 3 vision-language pre-training methods: GLoRIA [27], BioViL [25], and MedKLIP [21]. Among the evaluated methods, GLoRIA employs fine-grained semantic representations, BioViL adopts a text semantic enhancement method, and MedKLIP is a medical knowledge-enhanced approach. The results are plotted in Fig. 2. AFLoc outperforms all 3 comparative methods by a significant margin on both evaluation metrics. In terms of the IoU metric, AFLoc achieved 0.342 (95%CI: 0.333, 0.351), whereas GLoRIA, BioViL, and MedKLIP obtained 0.278 (95%CI: 0.270, 0.286), 0.250 (95%CI: 0.232, 0.246), and 0.317 (95%CI: 0.310, 0.325), respectively. In terms of the CNR metric (Extended Data Table 1.), AFLoc achieved 1.538 (95%CI: 1.496, 1.578), whereas GLoRIA, BioViL, and MedKLIP obtained 1.223 (95%CI: 1.179, 1.271), 0.934 (95%CI: 0.885, 0.964), and 1.030 (95%CI: 1.013, 1.050), respectively. These results confirmed that our AFLoc can better localize pneumonia in CXR when compared to existing state-of-the-art methods.

MS-CXR

In this section, we presented the experimental results of different methods for the localization of cardiopulmonary radiological findings in CXR using the MS-CXR dataset. MS-CXR offers pathology-specific descriptions including image bounding box labels paired with radiological text descriptions. This dataset introduces a significantly more demanding real-world vision-language inference task compared to the RSNA Pneumonia dataset.

Similarly, we compared the results of our proposed AFLoc with the 3 vision-language pre-training methods, GLoRIA [27], BioViL [25], and MedKLIP [21]. As shown in Fig. 2, AFLoc demonstrated a significant advantage over GLoRIA, BioViL, and MedKLIP for the localization of cardiopulmonary radiological findings in CXR.
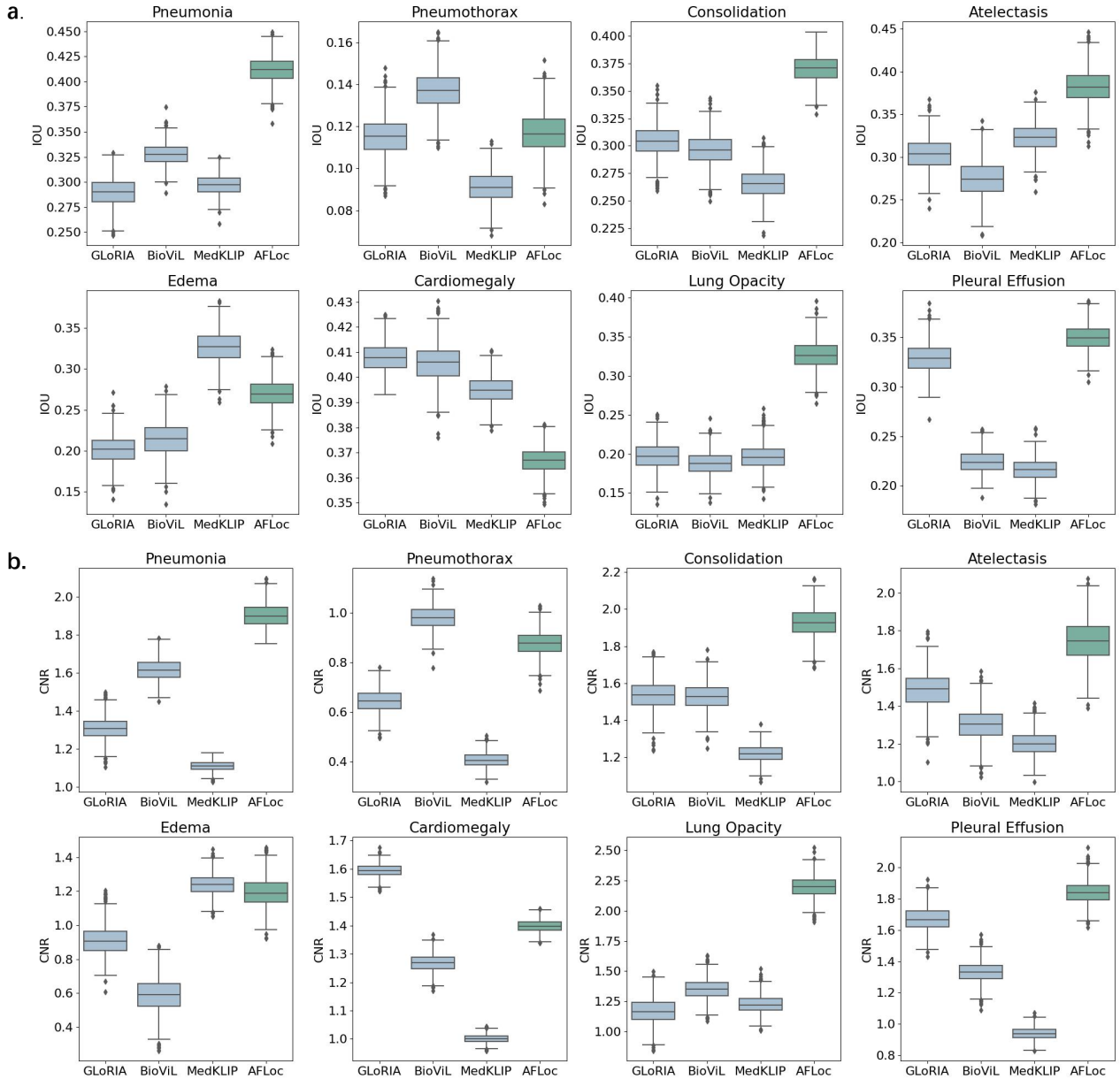
Fig. 3: Quantitative results of different models in localizing 8 distinct cardiopulmonary radiological findings, including pneumonia, pneumothorax, consolidation, atelectasis, edema, cardiomegaly, lung opacity, and pleural effusion, using the MS-CXR dataset. (a) shows the Intersection over Union (IoU) scores. (b) displays the Contrast-to-Noise ratio (CNR) scores.

Specifically, compared with GLoRIA (0.269; 95%CI: 0.242, 0.295), BioViL (0.258; 95%CI: 0.232, 0.285), and MedKLIP (0.264; 95%CI: 0.240, 0.287), our AFLoc (0.324; 95%CI: 0.298, 0.350) increased the IoU by more than 6%, 7%, and 6%, respectively. When carefully examining the results obtained by the different methods for the specific diseases (Fig. 3), it can be found that AFLoc showed significant improvements in all 8 diseases, especially in lung opacity (11%), pneumonia (8%), atelectasis (6%), and consolidation (7%), demonstrating its superiority and generalization.

Two different descriptive scenarios were evaluated using the MS-CXR dataset: simple and precise descriptions. Simple descriptions, as shown in Fig. 1, use the following template: findings suggesting {disease name}, where "disease name" is the name of the disease (e.g., pneumonia). Precise descriptions, on the other hand, come from the MS-CXR dataset. The descriptions provided by MS-CXR are not merely brief explanations but are real descriptions of radiological findings from original radiological reports and verbal records. One example description could be "Large right-sided pneumothorax, air space opacity in a right infrahilar location." These descriptions often carry important attributes and location information related to the disease. Since MedKLIP
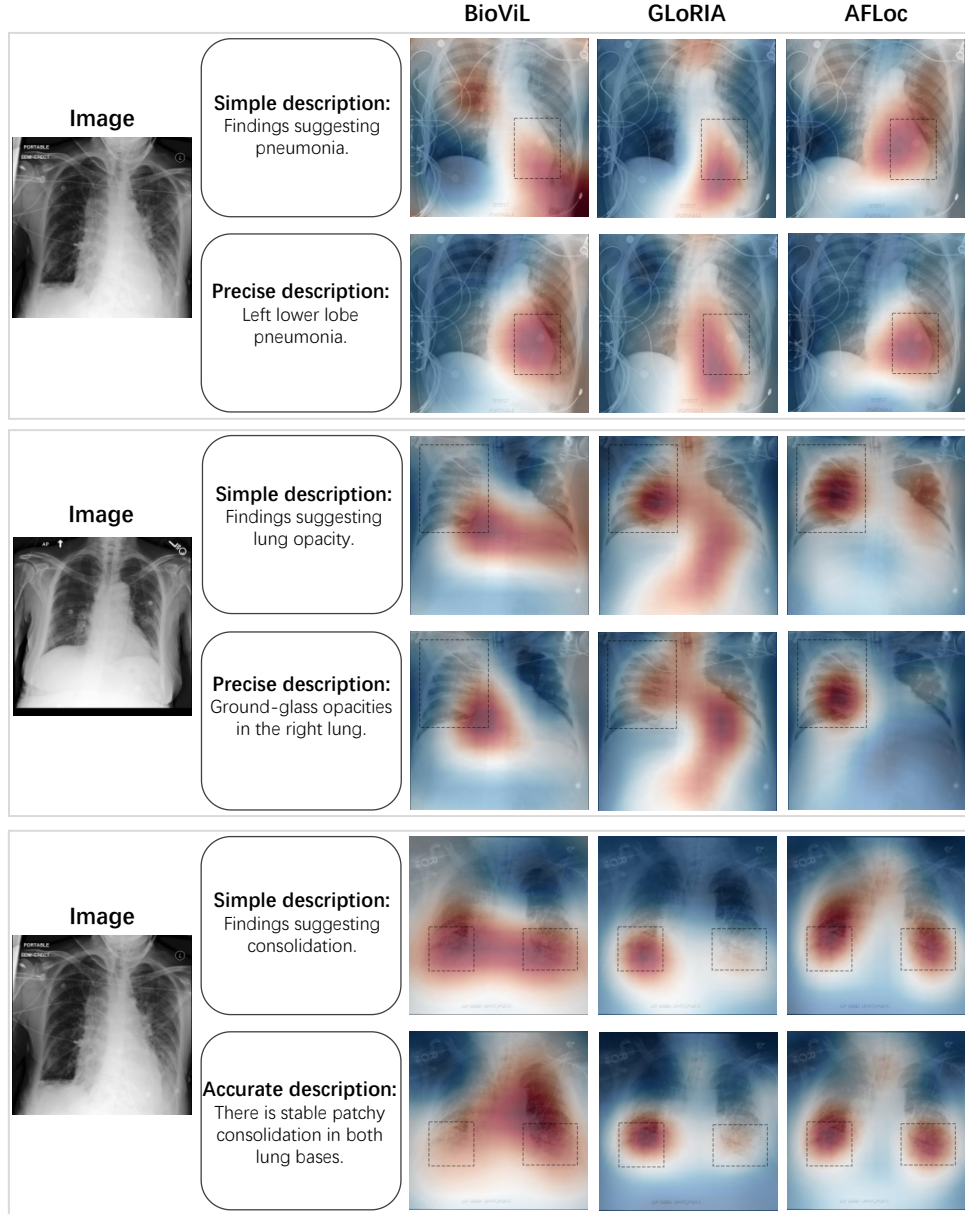
Fig. 4: Visualizations of pathological lesions localization by different models, BioViL, GLoRIA, and AFLoc, under two description scenarios: simple descriptions and precise descriptions. Black dashed boxes indicate the pathology areas marked by radiologists, and the intensity of red in the heatmaps signifies the focus level of the model's prediction, with deeper red indicating higher focus.

[21] employs a disease query mechanism, it is not applicable for this type of assessment. The results of testing under these two descriptive scenarios of the two comparative methods, GLoRIA and BioViL, as well as our proposed AFLoc, are listed in Table 1. Overall, precise descriptions effectively enhance the localization performance of all 3 methods, with AFLoc outperforming the two comparative methods under different conditions. Using simple descriptions, AFLoc obtains an IoU of 0.289 and a CNR of 1.350. With precise descriptions, AFLoc achieves an IoU of 0.324 and a CNR of 1.634. Example visualization results demonstrating the localization outcomes are plotted in Fig. 4. We can observe that all methods can somewhat find the diseased regions when precise descriptions are provided, with AFLoc achieving more accurate localization performance. When only simple descriptions are provided, AFLoc can still accurately locate the diseased areas, while the two comparative methods struggle to correctly locate the corresponding regions. Furthermore, in scenarios involving simple descriptions, the localization performance of AFLoc surpasses that of the two compared methods under precise descriptions.

Table 1: Quantitative results of different models on the MS-CXR dataset evaluated under two different descriptive scenarios. Numbers within parentheses indicate 95% CI.

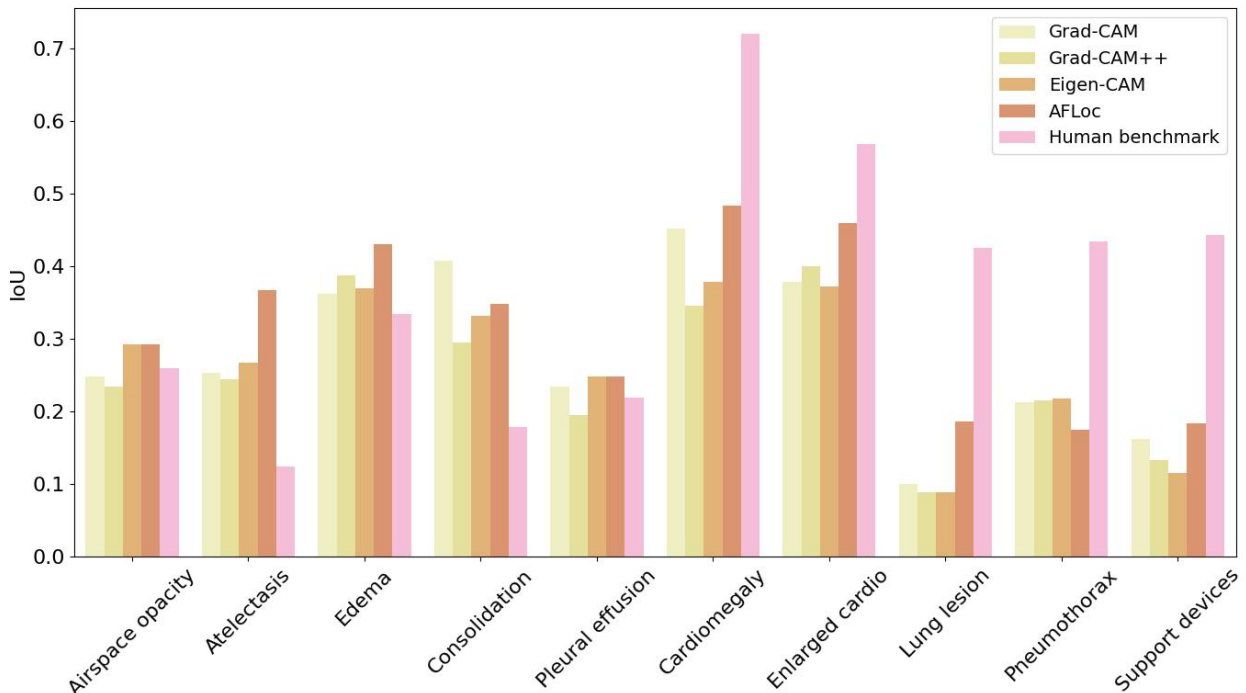|	GLoRIA	BioViL	AFLoc
IoU			
Simple description	0.240 (0.214,0.266)	0.229 (0.203,0.256)	0.289 (0.261,0.315)
Precise description	0.269 (0.242,0.295)	0.258 (0.232,0.285)	0.324 (0.298,0.350)
CNR			
Simple description	1.126 (1.000,1.252)	1.015 (0.894,1.132)	1.350 (1.216,1.489)
Precise description	1.289 (1.149,1.430)	1.247 (1.111,1.380)	1.634 (1.494,1.775)

Fig. 5: Quantitative results (IoU) of different methods on localizing 10 different pathologies using the CheXlocalize dataset.

CheXlocalize

Employing the CheXlocalize dataset, we compared AFLoc with 3 common saliency methods, Grad-CAM [18], Grad-CAM++ [19], and Eigen-CAM [20], and the human benchmark [17]. These saliency methods are trained under fixed categories and require image-level labels. They are used to generate heatmaps that highlight medical image regions most influential to deep neural network (DNN) predictions. Saliency methods are particularly useful in medical image analysis as they provide explainability of models, generating heatmaps without requiring bounding box annotations or pixel-level segmentation during training.

Fig. 5 presented the results of different methods for localizing pathologies using the CheXlocalize dataset. It is worth noting that AFLoc outperforms the saliency methods in most cases, despite not relying on image-level or location-level annotations, which are required by the saliency methods. AFLoc shows notable performance

improvements in localizing specific pathologies such as atelectasis (10%), lung lesions (9%), enlarged cardiomyopathy (6%) and edema (4%). The average IoU (0.318) achieved by AFLoc is about 4% higher than that of the best comparison method, Grad-CAM (0.282). Additionally, AFLoc surpasses the performance of the human benchmark in localizing 5 different pathologies (airspace opacity, atelectasis, edema, consolidation, and pleural effusion). These findings highlight the potential of AFLoc in the field of medical image analysis.

COVID Rural

The capability of a model to generalize to unseen diseases is very important in clinical applications. To assess this generalization ability, we evaluated different models (GLoRIA, BioViL, MedKLIP, and the proposed AFLoc) using the COVID Rural dataset, which was collected for COVID-19 detection. As all the models were trained using the dataset, which was collected before the emergence of COVID-19 and lacks information about the virus, their performance on the COVID Rural dataset can serve as a means to evaluate their capability to generalize to unseen diseases.

The quantitative results are plotted in Fig. 2 and listed in Extended Data Table 1. AFLoc (IoU: 0.212; 95%CI: 0.186, 0.234. CNR: 1.061; 95%CI: 0.948, 1.175) achieved superior performance compared to GLoRIA's (IoU: 0.139; 95%CI: 0.120, 0.157. CNR: 0.664; 95%CI: 0.561, 0.772), BioViL's (IoU: 0.164, 95%CI: 0.145, 0.183. CNR: 0.776; 95%CI: 0.698, 0.862), and MedKLIP's (IoU: 0.176; 95%CI: 0.157, 0.194. CNR: 0.841; 95%CI: 0.771, 0.907) in terms of both IoU and CNR metrics. These results indicated that AFLoc could better generalize to unseen disease, which could be a valuable characteristic when applied in clinical situations.

Adaptability to another medical imaging modality

To demonstrate AFLoc versatility as a general vision-language foundation model, we investigated its adaptability in its AI-driven pathological lesions localization capability to other medical image modalities. To exemplify this ability, we chose a common ophthalmology image modality retina fundus photographs. We trained and tested the model on 26,028 retinal images. We conducted an evaluation and compared the performance with other similar models. The quantitative results are listed in Extended Data Table 3. These results demonstrated effective pathological lesions localization and advantages over other current models, achieving superior performance compared to ConVIRT and GLoRIA models (Extended Data Table 3). Examples of images are illustrated in Extended Data Fig. 1-3. We tested the disease diagnostic performance on chest x-ray and fundus as shown in Extended Data Table 4 and Extended Data Table 5. These results indicated that AFLoc could adapt to a completely different medical image modality, which is valuable in clinical applications.

Ablation Study

In the ablation study, we explored the impact of using word-level, sentence-level, and report-level text embeddings on the performance of AFLoc. The results are listed in Extended Data Table 2. When using only one level of text embeddings, the performance of AFLoc deteriorates a lot, especially for word-level and report-level embeddings. One possible explanation could be that the word-level embeddings lack sufficient contextual information to capture the characteristics of the pathology, whereas the report-level embeddings may fail to capture critical diagnostic details due to their overly macroscopic perspective. On the other hand, AFLoc using sentence-level embeddings achieves relatively higher performance, suggesting that sentence-level embeddings can provide richer contextual information, which is important for pathological lesions localization in medical imaging.

When these different levels of text embeddings were combined in utilization, clear performance enhancement could be observed, and the best performance was achieved when all three levels were employed, fully supporting our hypothesis that the combination of multi-level information is crucial for improving the accuracy of pathological lesions localization in medical images.

Discussion

Despite the importance of deep learning-based pathological lesions localization in medical images for clinical applications, existing methods face critical challenges related to annotated data limitation, model generalization, or category limitations [9, 21]. Our work aims to develop an annotation-free deep learning model, AFLoc, for generalizable pathological lesions localization in chest X-rays through pre-training utilizing text and imaging. Extensive experiments validated that AFLoc can achieve outstanding pathological lesions localization performance, outperforming existing state-of-the-art medical vision-language pre-training methods (GLoRIA [27], BioViL [25], and MedKLIP [21]), in multiple datasets with different cardiopulmonary radiological findings including those not explicitly presented in the training data. This observed performance enhancement of AFLoc can be attributed mainly to its novel design of multi-level semantic structures, which effectively promote

the establishment of close correlations between complex medical concepts (text) and images at multiple granularities without requiring any annotations, facilitating the pathological lesions localization process. We further validated AFLoc generalization ability in retinal fundus image pathological lesion localization.

Specifically, AFLoc develops a multi-level semantic structure contrastive learning framework to achieve vision-language alignment at different levels of features. In contrast, most existing medical vision-language pre-training methods only use global information for contrastive learning [25] and ignore local details. It should be noted that pathology often occupies only a small part of the entire image. Thus, these global information-based models tend to struggle to accurately localize the pathology. Although some methods also adopted global and local text-image feature alignment [27], they often use words as the alignment units that lack complete semantic information, leading to inaccurate pathological lesions localization. In clinical practice, descriptions of pathologies are often expressed in sentences instead of just words, and sentences usually contain complete and detailed localizing information about the pathology. AFLoc was developed to fully explore the provided image and text information while following routine clinical practice. It utilizes word-level, sentence-level, and report-level text embeddings during pre-training, which can comprehensively capture the information important for pathological lesions localization.

In the meantime, thanks to the authors who provided the CheXlocalize dataset with corresponding benchmarking saliency methods [17], we were able to compare AFLoc with the 3 saliency methods, Grad-CAM [18], Grad-CAM++ [19], and Eigen-CAM [20], using this dataset. Saliency methods generate heatmaps that highlight the regions in a medical image that are most influential to DNN predictions. These methods are particularly useful in the context of medical imaging as they can provide post-hoc explainability of the models that were never exposed to bounding box annotations or pixel-level segmentation masks during training. Nevertheless, our AFLoc achieved better performance than all 3 comparative saliency methods when localizing most of the pathologies (7 out of 10) (Fig. 5). Additionally, although saliency methods do not require region-based (bounding box annotations or pixel-level segmentation masks) labels, they are trained using image-level pathological labels, and thus, they are limited to a closed set of pathology categories, limiting their applicability to those pathologies not presented in the training data. On the other hand, AFLoc does not require any image-level pathological labels, pixel-level segmentation masks, or bounding box annotations, and allows for the localization of any pathologies using text descriptions, demonstrating powerful generalization capabilities.

The significant advantage of AFLoc in localizing unseen pathologies (i.e., COVID-19) as demonstrated when evaluated on the COVID Rural dataset can be attributed to two key factors. First, the symptoms of COVID-19 in X-ray images, such as patchy shadows in the lungs, interstitial changes, and ground-glass opacities, are not unique to COVID-19 and can usually be observed in non-COVID-19 pneumonia cases as well [35, 36]. Therefore, although the utilized training dataset, MIMIC-CXR, lacks information about the COVID-19 virus, AFLoc can learn relevant pathological knowledge from the diagnostic reports and effectively apply it to diagnose this unseen disease. Second, compared to existing methods that simply match original reports with image scans [25] or use domain knowledge-enhanced approaches [21], AFLoc is more advanced and detailed. It focuses on mining the hierarchical information in images and reports and implicitly learns the complex relationships between different levels of features. Through this design, AFLoc can deeply understand and differentiate the subtle differences between various radiological findings, thereby achieving higher accuracy and effectiveness in the localization of unseen pathologies.

Moreover, AFLoc was designed to be prompt-flexible and can achieve accurate pathological lesions localization when provided with either rough prompts or detailed prompts. Particularly, AFLoc can effectively localize pathological regions in an image even when provided with simple or incomplete text prompts (Fig. 4). Besides, when more detailed and accurate textual descriptions are provided, such as those describing the specific symptoms of a pathology, the pathological lesions localization accuracy of AFLoc can be accordingly improved (Fig. 4). This flexibility of AFLoc is particularly important for its application in complex and variable medical situations, as it allows the system to better serve different diagnostic needs and clinical contexts.

Despite all these clinically valuable characteristics of AFLoc, it also has some limitations. Firstly, although AFLoc has outperformed existing medical vision-language pre-training methods and saliency methods for pathological lesions localization, there is still room for improvement to achieve precise pathology segmentation. Secondly, the training dataset we used is relatively small, especially when compared to those available in the natural image domain. With larger training datasets, the performance of AFLoc can be further improved. Finally, the current model cannot correct possible errors in the provided text prompts or provide more detailed pathological descriptions and etiological analyses. In the future, we plan to explore more in these directions to make AFLoc more effective and comprehensive.

In summary, we have developed an annotation-free vision-language pre-training model, AFLoc, that can generalize well to localize various pathologies in both chest X-rays and retina fundus images provided by corresponding pathologies text descriptions. Extensive experimental results show that AFLoc can outperform existing

state-of-the-art medical vision-language pre-training methods and saliency methods, highlighting its immense potential in real-world clinical applications where a large amount of unannotated data exists.

Methods

Dataset

All models were pre-trained using X-ray images and clinical reports from the MIMIC-CXR dataset and subsequently evaluated on 4 external datasets: RSNA Pneumonia, MS-CXR, CheXlocalize, and COVID Rural. These 4 datasets offer annotations with bounding boxes or pixel-level labels provided by professional radiologists, enabling the assessment of pathological lesions localization performance.

MIMIC-CXR [33]. The MIMIC-CXR dataset is an extensive, publicly available collection of chest X-ray images, paired with free-text radiological reports. It contains 377,110 images that are linked to 227,835 radiological studies. Each study within the database may consist of one or more images, providing a diverse range of scanning perspectives for analysis and research purposes.

RSNA Pneumonia [30]. The RSNA Pneumonia dataset presents a challenge in identifying visual signals of pneumonia from medical images. Images in this dataset are accompanied by bounding box labels that indicate the areas affected by pneumonia. Over 1000 cases in this dataset are positive, with each image potentially containing one or more boundary boxes highlighting the pneumonia regions.

MS-CXR [25]. MS-CXR is a curated database that features 1,153 image-sentence pairs of bounding boxes along with their corresponding phrases. This collection encompasses 8 different types of cardiopulmonary radiological findings. The image-sentence pairs are distributed equally among the 8 findings. In addition to brief descriptions, this dataset provides authentic depictions of radiological findings as described in radiology reports and oral records. All the data have been annotated and validated by professional radiologists, ensuring a gold standard for phrase grounding assessment. MS-CXR is a subset of the MIMIC-CXR dataset. All data in MS-CXR have been removed from the MIMIC-CXR training set to ensure it was not used in the pre-training process.

CheXlocalize [17]. The CheXlocalize dataset is a comprehensively curated chest X-ray dataset. It features multi-label, pixel-level segmentations meticulously drawn by two board-certified radiologists, ensuring a highly precise ground truth annotation for each image. This dataset includes 234 images, encompassing 643 segmented pathologies. It covers a broad range of cardiopulmonary conditions, including airspace opacity, atelectasis, cardiomegaly, consolidation, edema, enlarged cardiomediastinum, lung lesion, pleural effusion, pneumothorax, and support devices. Moreover, CheXlocalize also provides human benchmark segmentations, drawn by a separate group of 3 board-certified radiologists, which can be used to study human benchmark localization performance.

COVID Rural [31, 32]. The COVID Rural project includes 221 chest X-ray images from 105 patients who tested positive for COVID-19. In these images, opaque areas associated with COVID-19 infection are delineated by polygons that connect specific points. The manual annotations of these images were generated by primary physicians and reviewed by experienced radiologists.

SIIM-ACR Pneumothorax Segmentation (SIIM) [37]. The SIIM dataset is designed to promote the development of models for identifying pneumothorax. It includes more than 120,000 frontal chest X-rays, each of which has been precisely annotated. Employing the data partitioning method described by [27], we conducted tests on the test set.

Retinal fundus photographs. This dataset was compiled from a total of 26,028 fundus images and paired reports from 11,372 individuals. The training set and internal validation set comprised fundus images captured by Zeiss fundus cameras. We divided the data set into training, validation and testing sets by 8:1:1 based on the patient's unique ID, which ensure that the same patient does not appear in the same data set. Our model was trained and validated on the training and validation sets, respectively, and model performance evaluations were done on the testing dataset. To evaluate the performance of our model in pathological lesions localization, we utilized an additional dataset for validation, which was annotated at the pixel level by retinal specialists of 10 years of experience. Specifically, this dataset includes 437 images of neovascularization, 160 images of drusen, and 498 images of retinal hemorrhage.

Approvals for the research were secured from the Institutional Review Board/Ethics Committees of all participating hospitals or institutes. Consent forms were signed by all involved patients. The study was carried out in accordance with the United States Health Insurance Portability and Accountability Act. Furthermore, it was in compliance with the principles of the Declaration of Helsinki, and conformed to policies of the Chinese Center for Disease Control and Prevention, as well as the Chinese Health Laws.

The Proposed AFLoc Model

Text encoding. The original radiology reports usually include a "Findings" section, detailing clinical observations, and an "Impressions" section. These sections typically contain multiple sentences. In GLoRIA [27], a block tokenization technique was used, constructing complete words by aggregating multiple subwords. On the other hand, BioViL [25] employs a custom dictionary developed from multiple datasets, aiming to reduce the frequency of words being split into subwords. A radiological finding in an image might require information of location, size, and severity for a comprehensive description. Treating words as independent entities may overlook the complete semantics, leading to incorrect semantic alignment between text and image. In our proposed AFLoc, text embeddings are extracted at three levels: word-level, sentence-level, and report-level, aiming to represent report content more comprehensively and precisely through multi-granularity semantics. Additionally, this three levels structure is naturally present in the text, requiring no complex designs to accomplish our text encoding.

Specifically, we employ BioClinicalBERT [38] as our text encoder to extract text embeddings. When processing a medical report x_t containing Q words and P sentences, each word is tokenized into q_i tokens. The tokenizer inputs the tokenized report into the text encoder $e_t^I \in \mathbb{R}^H$, where H is the maximum token length. The text encoder outputs $e_t^O \in \mathbb{R}^{L \times H \times D}$, where B represents the batch size, L is the number of layers, and D indicates the feature dimension. We take the average embedding of the last 4 layers as the subword-level embedding $t_{sub} \in \mathbb{R}^{H \times D}$. Then, we aggregate embeddings at the word, sentence, and report levels. Particularly, for a word, all its subword-level embeddings are summarized to obtain Q the word-level embeddings t_w. On the other hand, all corresponding subword-level embeddings are averaged to obtain P sentence-level embeddings t_s and one report-level embedding t_r.

Image encoding. We adopt a popular architecture, ResNet-50 [39], as the backbone of our image encoder E_v. When processing the input image x_v, we extract image features from specific intermediate convolutional layers from the image encoder. Shallow features are extracted from the third down-sampling stage, and deep features are from the fourth down-sampling stage. Additionally, the features from the last convolutional layer of ResNet-50 are average pooled to obtain the global image features. Then, we use two 1×1 convolutions and a linear layer to adjust the dimensions of the three different levels of image features to match the text feature dimensions. We obtain shallow features $v_s \in \mathbb{R}^{D \times M}$, deep features $v_d \in \mathbb{R}^{D \times \frac{M}{4}}$, and global features $v_g \in \mathbb{R}^D$, where M denotes the number of sub-regions in shallow features, and D represents the feature dimension.

Multi-level semantic alignment. Given that medical reports usually provide detailed descriptions corresponding to the observations in medical images, the images and their corresponding reports should exhibit consistent semantic properties in the multimodal feature space. This inspires us to perform semantic alignment between image features and text embeddings at the three levels of different granularities. Specifically, shallow and deep image features extracted by the image encoder are aligned with the word-level and sentence-level text embeddings extracted by the text encoder for local semantic alignment, while the global image features and the report-level text embeddings are aligned for global semantic alignment. The detailed process is depicted in Fig. 1.

For local semantic alignment, we adopt the localized feature matching function $Z(\cdot, \cdot)$ [27]. Taking sentence embeddings as an example, the similarity matrix between P sentences and $M/4$ image sub-regions is represented as:

$$s = v_d^T t_s \tag{1}$$

The image feature representation, weighted by sentences c_i and localized feature matching function $Z(\cdot, \cdot)$ are represented as:

$$c_i = \sum_{j=1}^{\frac{M}{4}} log \frac{exp(s_{ij})/\tau_1}{\sum_{k=1}^{\frac{M}{4}} exp(s_{ik})/\tau_1} v_{dj} \tag{2}$$

$$Z(c, t) = log(\sum_{i=1}^{N} exp(\Phi(c_i, t_i)/\tau_2)) \tag{3}$$

τ_1 and τ_2 are scaling factors, and N represents the size of the first dimension of the local embeddings (i.e., P for sentence-level embeddings). $\Phi(c_i, t_i)$ is used to calculate the cosine similarity between the two vectors (c_i, t_i). The local contrastive loss between deep features and sentence-level embeddings is defined as:

$$L_{ds} = -\frac{1}{B} \sum_{i}^{B} \left(log \frac{exp(Z(v_d^i, t_s^i)/\tau_3)}{\sum_{k=1}^{B} exp(Z(v_d^i, t_s^k)/\tau_3)} + log \frac{exp(Z(v_d^i, t_s^i)/\tau_3)}{\sum_{k=1}^{B} exp(Z(v_d^k, t_s^i)/\tau_3)} \right) \tag{4}$$

where τ_3 is a temperature parameter and B is the batch size. Similarly, we obtain the contrastive loss between shallow features and word-level embeddings:

$$L_{sw} = -\frac{1}{B}\sum_i^B \left(log \frac{exp(Z(v_s^i, t_w^i)/\tau_3)}{\sum_{k=1}^B exp(Z(v_s^i, t_w^k)/\tau_3)} + log \frac{exp(Z(v_s^i, t_w^i)/\tau_3)}{\sum_{k=1}^B exp(Z(v_s^k, t_w^i)/\tau_3)} \right) \quad (5)$$

For global semantic alignment, we optimize the global features and report-level embeddings by using paired and unpaired samples of images and texts according to the following loss function:

$$L_{gr} = -\frac{1}{B}\sum_i^B \left(log \frac{exp(\Phi(v_g^i, t_r^i)/\tau_3)}{\sum_{k=1}^B exp(\Phi(v_g^i, t_r^k)/\tau_3)} + log \frac{exp(\Phi(v_g^i, t_r^i)/\tau_3)}{\sum_{k=1}^B exp(\Phi(v_g^k, t_r^i)/\tau_3)} \right) \quad (6)$$

AFLoc is trained to jointly optimize the local and global semantic alignment. The final loss function for AFLoc is:

$$L = L_{sw} + L_{ds} + L_{gr} \quad (7)$$

Pathological lesions localization pipeline. After the pre-training phase, we transform the pathological lesions localization task into a text-image matching problem by providing text prompts (see Fig. 1c). These text prompts can follow a simple description template, such as: "Findings suggesting pathology" or adopt a detailed description of the pathology, like "Large right-sided pneumothorax, air space opacity in a right infrahilar location" provided by the MS-CXR dataset. The input text is passed to the text encoder to obtain sentence-level embeddings. For each input image, we use the image encoder to extract deep features, which are treated as local features. Next, by calculating the similarity between the text embeddings and image local feature vectors, we can generate a similarity map correlating the text prompt (pathology information) to the image. This similarity map is then upsampled to the original image size through bilinear interpolation. After normalization to the range of [-1, 1] and binarization using a threshold, the similarity map can be treated as the segmentation mask of the image that can localize the pathology.

Experimental details. For the MIMIC-CXR dataset, we preprocessed all chest X-ray images to a uniform size of 224×224 pixels and performed normalization. In our study, we focused on using a subset of the data that contains 249,262 frontal chest X-ray images and their corresponding textual descriptions. For the fundus image dataset, we adopted the same image preprocessing strategy as for MIMIC-CXR.

Typically, medical reports include "Findings" and "Impressions" sections. In our pretraining data, we used the content of these two sections as training text to train our model. During training, we employed random shuffling and sentence sampling methods to further enhance the textual data. Moreover, for the fundus dataset, we performed additional sentence augmentation to increase the diversity of medical reports. Specifically, we performed text augmentation on frequently occurring sentences in the reports, generating five semantically equivalent but differently expressed sentences for each sentence. During the training phase, these equivalent sentences were randomly replaced.

To train AFLoc, we used the Adam optimizer with an initial learning rate of 0.00002 and a momentum value of 0.9. Additionally, we implemented a learning rate decay mechanism, reducing the learning rate to 0.9 of its previous value after each epoch. All the hyperparameters, including batch size and learning rate, were optimized using the MIMIC-CXR validation dataset. The best model was obtained after training for 5 epochs with a batch size of 128.

Comparative Methods

Medical vision-language pre-training methods. Four medical vision-language pre-training methods were compared in this study, including ConVIRT [40], GLoRIA [27], BioViL [25], and MedKLIP [21]. ConVIRT improves visual representations by maximizing the agreement between true image-text pairs versus random pairs via a bidirectional contrastive objective between the image and text modalities. GLoRIA proposes an attention-based framework that learns global and local representations by comparing subregions of images with words in paired reports. BioViL achieves better text modeling by adopting an improved lexicon and innovative language pre-training methods. Then, contrastive learning is utilized with paired text and images. MedKLIP first extracts medical information from radiology reports through a triplet extraction module. Then, it uses a Transformer-based fusion model to combine this information and visual signals at the image block level, enhancing the capability of medical diagnostics. These 4 methods were employed in our study as state-of-the-art medical vision-language pre-training comparative methods.

Saliency methods. In addition to medical vision-language pre-training methods, 3 comparative saliency methods were also adopted in our study. Grad-CAM [18] uses the gradients flowing into the final convolutional layer for any target category to generate a coarse localization map, highlighting the important areas in the image used for classification. Grad-CAM++ [19] is an extension of Grad-CAM that aims to enhance and refine the visualization of the decision-making process of convolutional neural networks. Compared to the original Grad-CAM approach, Grad-CAM++ can provide clearer and more detailed visual explanations, especially in identifying specific classes in recognition models. Eigen-CAM [20] is a visualization technique to interpret the decisions of convolutional neural networks. It extends the traditional Class Activation Mapping (CAM) method, aiming to offer a more intuitive and detailed visual interpretation. The core idea of Eigen-CAM is to use principal component analysis to extract significant features from the outputs of the convolutional layers.

Acknowledgments

Data availability

MIMIC-CXR data is available at https://physionet.org/content/mimic-cxr/2.0.0 for users with credentialed access. RSNA Pneumonia data is available at https://www.rsna.org/rsnai/ai-image-challenge/RSNA-Pneumonia-Detection-Challenge-2018. MS-CXR data is available at https://physionet.org/content/ms-cxr/0.1/. CheXlocalize data is available at https://stanfordaimi.azurewebsites.net/datasets/abfb76e5-70d5-4315-badc-c94dd82e3d6d. COVID Rural data is available at https://www.cancerimagingarchive.net/collection/covid-19-ar/.

Code availability

The code is available on GitHub at https://github.com/YH0517/AFLoc.

References

[1] Coudray, N. *et al.* Classification and mutation prediction from non–small cell lung cancer histopathology images using deep learning. *Nature medicine* **24**, 1559–1567 (2018).

[2] Wang, P. *et al.* Development and validation of a deep-learning algorithm for the detection of polyps during colonoscopy. *Nature biomedical engineering* **2**, 741–748 (2018).

[3] Campanella, G. *et al.* Clinical-grade computational pathology using weakly supervised deep learning on whole slide images. *Nature medicine* **25**, 1301–1309 (2019).

[4] Courtiol, P. *et al.* Deep learning-based classification of mesothelioma improves prediction of patient outcome. *Nature medicine* **25**, 1519–1525 (2019).

[5] Lee, S. Y. *et al.* Localization-adjusted diagnostic performance and assistance effect of a computer-aided detection system for pneumothorax and consolidation. *npj Digital Medicine* **5**, 107 (2022).

[6] Cao, K. *et al.* Large-scale pancreatic cancer detection via non-contrast ct and deep learning. *Nature Medicine* 1–11 (2023).

[7] Song, Z. *et al.* Clinically applicable histopathological diagnosis system for gastric cancer detection using deep learning. *Nature communications* **11**, 4294 (2020).

[8] Leon, R. *et al.* Hyperspectral imaging benchmark based on machine learning for intraoperative brain tumour detection. *NPJ Precision Oncology* **7**, 119 (2023).

[9] Tiu, E. *et al.* Expert-level detection of pathologies from unannotated chest x-ray images via self-supervised learning. *Nature Biomedical Engineering* **6**, 1399–1406 (2022).

[10] Zhou, Y. *et al.* A foundation model for generalizable disease detection from retinal images. *Nature* **622**, 156–163 (2023).

[11] Kobayashi, H., Cheveralls, K. C., Leonetti, M. D. & Royer, L. A. Self-supervised deep learning encodes high-resolution features of protein subcellular localization. *Nature methods* **19**, 995–1003 (2022).

[12] Park, S. *et al.* Self-evolving vision transformer for chest x-ray diagnosis through knowledge distillation. *Nature communications* **13**, 3848 (2022).

[13] Zhou, H.-Y. *et al.* Generalized radiograph representation learning via cross-supervision between images and free-text radiology reports. *Nature Machine Intelligence* **4**, 32–40 (2022).

[14] Reed, C. J. *et al.* Self-supervised pretraining improves self-supervised pretraining. *Proceedings of the IEEE/CVF Winter Conference on Applications of Computer Vision* 2584–2594 (2022).

[15] He, K., Fan, H., Wu, Y., Xie, S. & Girshick, R. Momentum contrast for unsupervised visual representation learning. *Proceedings of the IEEE/CVF conference on computer vision and pattern recognition* 9729–9738 (2020).

[16] Chen, T., Kornblith, S., Norouzi, M. & Hinton, G. A simple framework for contrastive learning of visual representations. *International conference on machine learning* 1597–1607 (2020).

[17] Saporta, A. *et al.* Benchmarking saliency methods for chest x-ray interpretation. *Nature Machine Intelligence* **4**, 867–878 (2022).

[18] Selvaraju, R. R. *et al.* Grad-cam: Visual explanations from deep networks via gradient-based localization. *2017 IEEE International Conference on Computer Vision (ICCV)* 618–626 (2017).

[19] Chattopadhay, A., Sarkar, A., Howlader, P. & Balasubramanian, V. N. Grad-cam++: Generalized gradient-based visual explanations for deep convolutional networks. *2018 IEEE Winter Conference on Applications of Computer Vision (WACV)* 839–847 (2018).

[20] Muhammad, M. B. & Yeasin, M. Eigen-cam: Class activation map using principal components. *2020 international joint conference on neural networks (IJCNN)* 1–7 (2020).

[21] Wu, C., Zhang, X., Zhang, Y., Wang, Y. & Xie, W. Medklip: Medical knowledge enhanced language-image pre-training. *Proceedings of the IEEE/CVF International Conference on Computer Vision* (2023).

[22] Morens, D. M. & Fauci, A. S. Emerging infectious diseases: threats to human health and global stability. *PLoS pathogens* **9**, e1003467 (2013).

[23] Yan, B. & Pei, M. Clinical-bert: Vision-language pre-training for radiograph diagnosis and reports generation. *Proceedings of the AAAI Conference on Artificial Intelligence* **36**, 2982–2990 (2022).

[24] Bannur, S. *et al.* Learning to exploit temporal structure for biomedical vision-language processing. *Proceedings of the IEEE/CVF Conference on Computer Vision and Pattern Recognition* 15016–15027 (2023).

[25] Boecking, B. *et al.* Making the most of text semantics to improve biomedical vision–language processing. *European conference on computer vision* 1–21 (2022).

[26] Zhang, Y., Jiang, H., Miura, Y., Manning, C. D. & Langlotz, C. P. Contrastive learning of medical visual representations from paired images and text. *Machine Learning for Healthcare Conference* 2–25 (2022).

[27] Huang, S.-C., Shen, L., Lungren, M. P. & Yeung, S. Gloria: A multimodal global-local representation learning framework for label-efficient medical image recognition. *Proceedings of the IEEE/CVF International Conference on Computer Vision* 3942–3951 (2021).

[28] Zhou, H.-Y., Lian, C., Wang, L. & Yu, Y. Advancing radiograph representation learning with masked record modeling. *The Eleventh International Conference on Learning Representations* (2023).

[29] Franquet, T. Imaging of community-acquired pneumonia. *Journal of thoracic imaging* **33**, 282–294 (2018).

[30] Shih, G. *et al.* Augmenting the national institutes of health chest radiograph dataset with expert annotations of possible pneumonia. *Radiology: Artificial Intelligence* **1**, e180041 (2019).

[31] Desai, S. *et al.* Chest imaging representing a covid-19 positive rural us population. *Scientific data* **7**, 414 (2020).

[32] Tang, H., Sun, N., Li, Y. & Xia, H. Deep learning segmentation model for automated detection of the opacity regions in the chest x-rays of the covid-19 positive patients and the application for disease severity. *medRxiv* 2020–10 (2020).

[33] Johnson, A. E. *et al.* Mimic-cxr, a de-identified publicly available database of chest radiographs with free-text reports. *Scientific data* **6**, 317 (2019).

[34] Rezatofighi, H. *et al.* Generalized intersection over union: A metric and a loss for bounding box regression. *Proceedings of the IEEE/CVF conference on computer vision and pattern recognition* 658–666 (2019).

[35] Bernheim, A. *et al.* Chest ct findings in coronavirus disease-19 (covid-19): relationship to duration of infection. *Radiology* **295**, 685–691 (2020).

[36] Wong, H. Y. F. *et al.* Frequency and distribution of chest radiographic findings in patients positive for covid-19. *Radiology* **296**, E72–E78 (2020).

[37] Anna, Z. *et al.* Siim-acr pneumothorax segmentation (2019). URL https://kaggle.com/competitions/siim-acr-pneumothorax-segmentation.

[38] Alsentzer, E. *et al.* Publicly available clinical bert embeddings. *NAACL HLT 2019* 72 (2019).

[39] He, K., Zhang, X., Ren, S. & Sun, J. Deep residual learning for image recognition. *Proceedings of the IEEE conference on computer vision and pattern recognition* 770–778 (2016).

[40] Zhang, Y., Jiang, H., Miura, Y., Manning, C. D. & Langlotz, C. P. Contrastive learning of medical visual representations from paired images and text 2–25 (2022).

Appendix A

Extended Data Table 1: Quantatitive pathological lesions localization results (CNR) of different models on the 3 datasets, RSNA Pneumonia [30], COVID Rural [31, 32], MS-CXR [25]. Numbers within parentheses indicate 95% CI.

Methods	RSNA Pneumonia	Covid-Rural	MS-CXR
GLoRIA	1.223 (1.179,1.271)	0.664 (0.561,0.772)	1.289 (1.149,1.430)
BioViL	0.934 (0.885,0.964)	0.776 (0.698,0.862)	1.247 (1.111,1.380)
MedKLIP	1.030 (1.013,1.050)	0.841 (0.771,0.907)	1.043 (0.962,1.131)
AFLoc	**1.538 (1.496,1.578)**	**1.061 (0.948,1.175)**	**1.634 (1.494,1.775)**

Extended Data Table 2: Quantitative results (IoU) from the ablation study to investigate the importance of the different levels of text embeddings.

Word-level	Sentence-level	Report-level	RSNA Pneumonia	COVID Rural	MS-CXR	CheXlocalize	Mean
✓			0.239	0.147	0.180	0.133	0.175
	✓		0.281	0.169	0.318	0.301	0.267
		✓	0.191	0.056	0.105	0.186	0.135
✓	✓		0.329	0.177	0.264	0.285	0.264
✓		✓	0.254	0.159	0.175	0.200	0.197
	✓	✓	0.285	0.211	**0.325**	0.305	0.282
✓	✓	✓	**0.342**	**0.212**	0.324	**0.318**	**0.299**

Extended Data Table 3: Quantitative results of different models on the retina photograph dataset evaluated under two different evaluation metrics. Numbers within parentheses indicate 95% CI.

Methods	Neovascularization	Drusen	Intraretinal hemorrhage	Mean	Metrics
ConVIRT	0.130 (0.117, 0.142)	0.120 (0.099, 0.142)	0.079 (0.074, 0.084)	0.110 (0.097, 0.123)	IoU
GLoRIA	0.143 (0.131, 0.155)	0.107 (0.087, 0.131)	0.075 (0.070, 0.080)	0.108 (0.096, 0.122)	IoU
AFLoc	**0.321** **(0.303, 0.337)**	**0.147** **(0.123, 0.173)**	**0.097** **(0.091, 0.103)**	**0.188** **(0.172, 0.204)**	IoU
ConVIRT	0.361 (0.277, 0.439)	0.654 (0.527, 0.790)	0.255 (0.232, 0.278)	0.423 (0.345, 0.502)	CNR
GLoRIA	0.498 (0.43, 0.57)	0.655 (0.516, 0.789)	0.215 (0.195, 0.237)	0.458 (0.380, 0.532)	CNR
AFLoc	**1.454** **(1.372, 1.526)**	**0.929** **(0.790, 1.064)**	**0.372** **(0.349, 0.395)**	**0.918** **(0.837, 0.995)**	CNR

Extended Data Table 4: Comparison of Area Under the Curve (AUC) scores with other state-of-the-art methods on the zero-shot classification task, evaluating diagnostic imaging analysis performance.

Methods	RSNA Pneumonia	SIIM
ConVIRT	0.804	0.643
GLoRIA	0.715	0.534
BioViL	0.828	0.708
CheXzero	0.858	0.688
MedKLIP	0.869	0.892
AFLoc	**0.887**	**0.897**

Extended Data Table 5: Comparative performance metrics of self-supervised and supervised learning methods on ophthalmic disease classification tasks, detailing the Area Under the Curve (AUC) for Macular Degeneration (MD), Retinopathy, Myopia, Glaucoma, Congenital Optic Disc Anomalies (CODA), and Retinal Arteriosclerosis (RAS) across varying label availability scenarios.

Methods	Label fraction	MD	Retinopathy	Myopia	Glaucoma	CODA	RAS	Mean
Self-supervised								
ConVIRT	0%	0.421	0.759	0.870	0.848	0.854	0.466	0.703
GLoRIA	0%	0.914	0.592	0.774	0.926	0.803	0.636	0.774
AFLoc	0%	**0.978**	**0.839**	**0.962**	**0.938**	**0.899**	**0.643**	**0.877**
Supervised								
AFLoc-w/o pretraining	100%	0.794	0.749	0.962	0.921	0.934	0.907	0.878
AFLoc-w/ pretraining	10%	0.955	0.916	**0.998**	**0.996**	**0.999**	**0.999**	0.977
AFLoc-w/ pretraining	100%	**0.992**	**0.978**	**0.998**	0.992	**0.999**	**0.999**	**0.993**
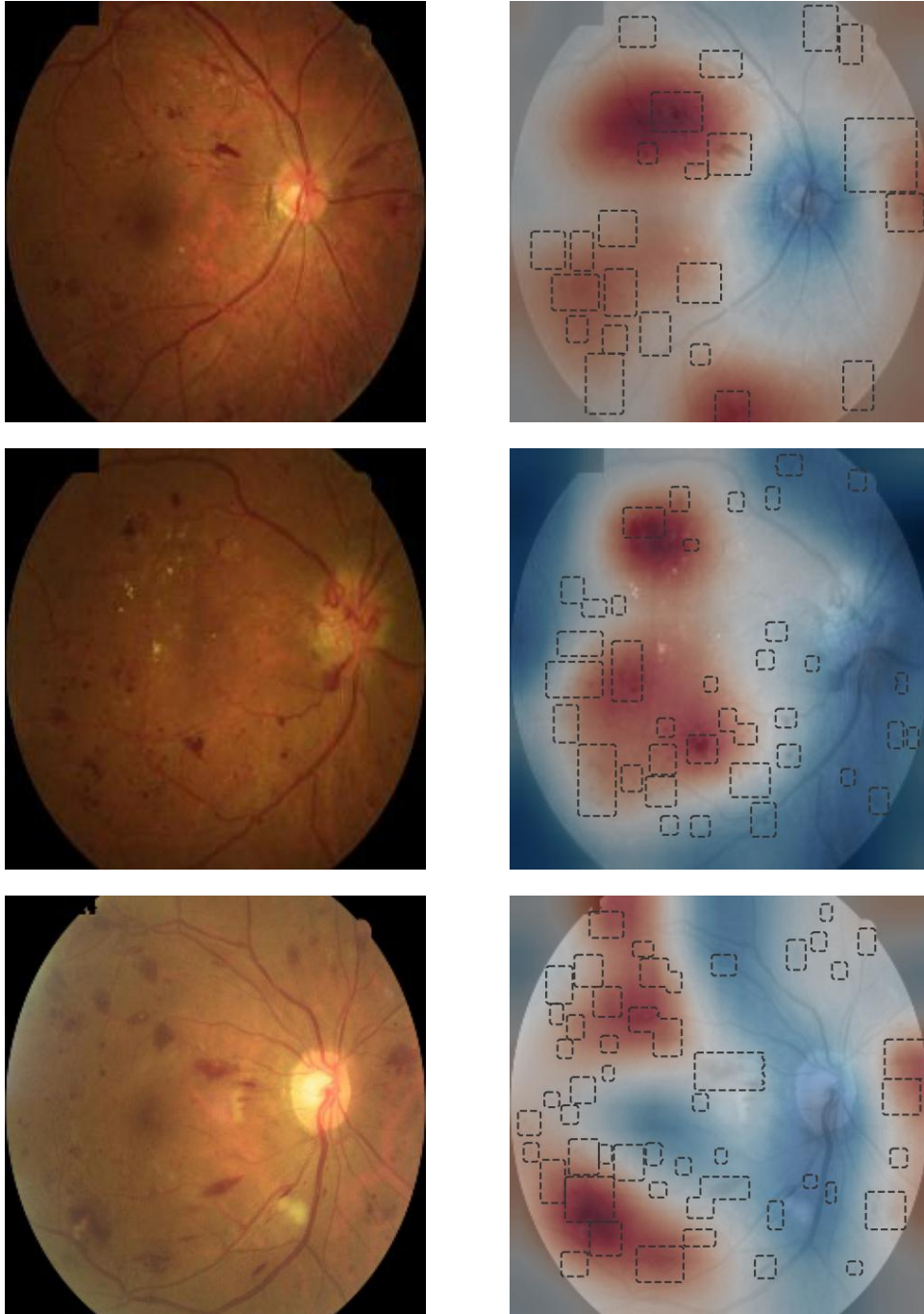
Extended Data Figure 1: Visualizations of pathology localization by AFLoc on retinal fundus photographs of **retinal hemorrhages**. Black dashed polygens indicate the pathology areas marked by eye doctors, and the intensity of red in the heatmaps signifies the focus level of the model's prediction, with deeper red indicating higher focus.
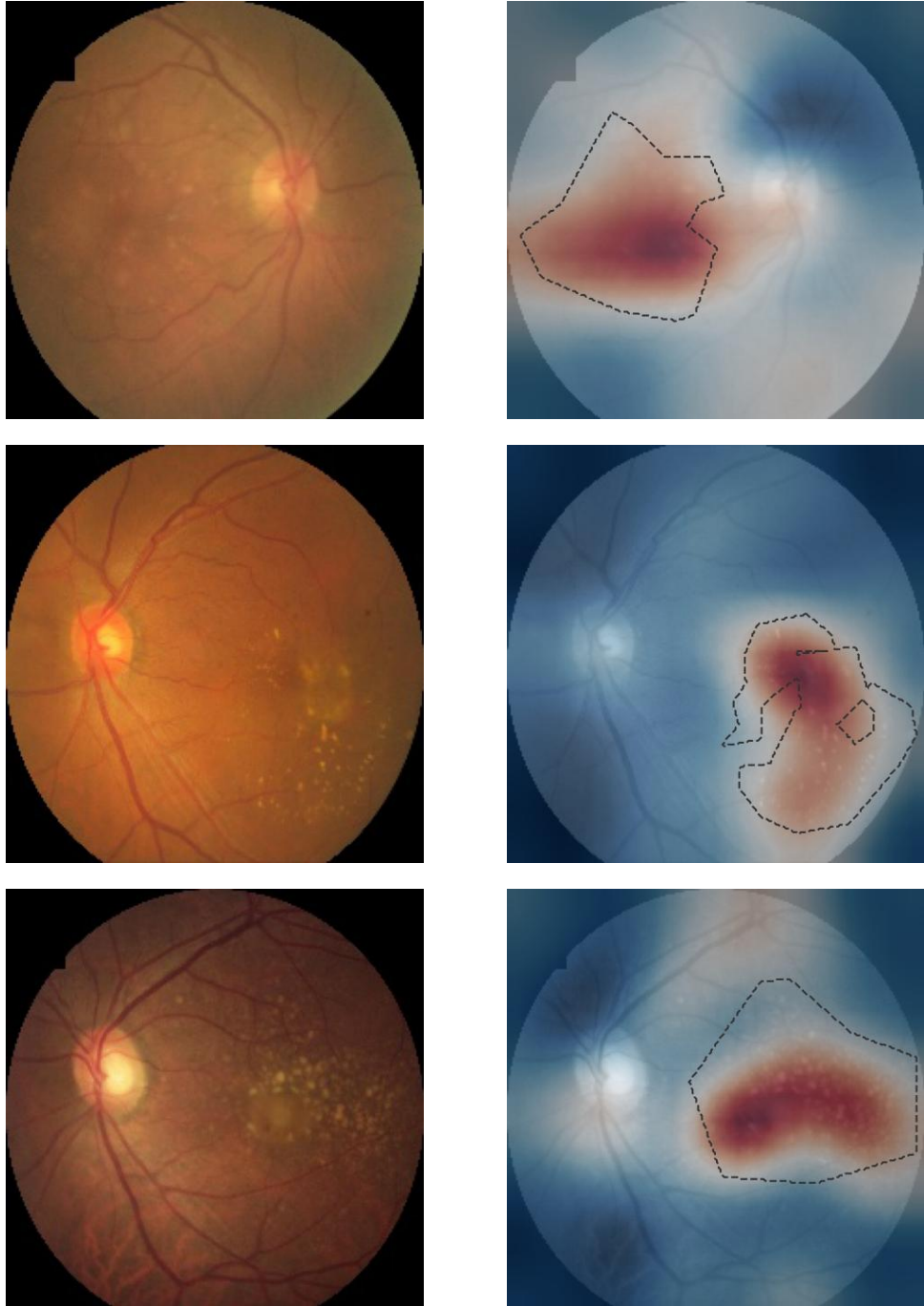
Extended Data Figure 2: Visualizations of pathology localization by AFLoc on retinal fundus photographs of **drusen**. Black dashed polygons indicate the pathology areas marked by eye doctors, and the intensity of red in the heatmaps signifies the focus level of the model's prediction, with deeper red indicating higher focus.
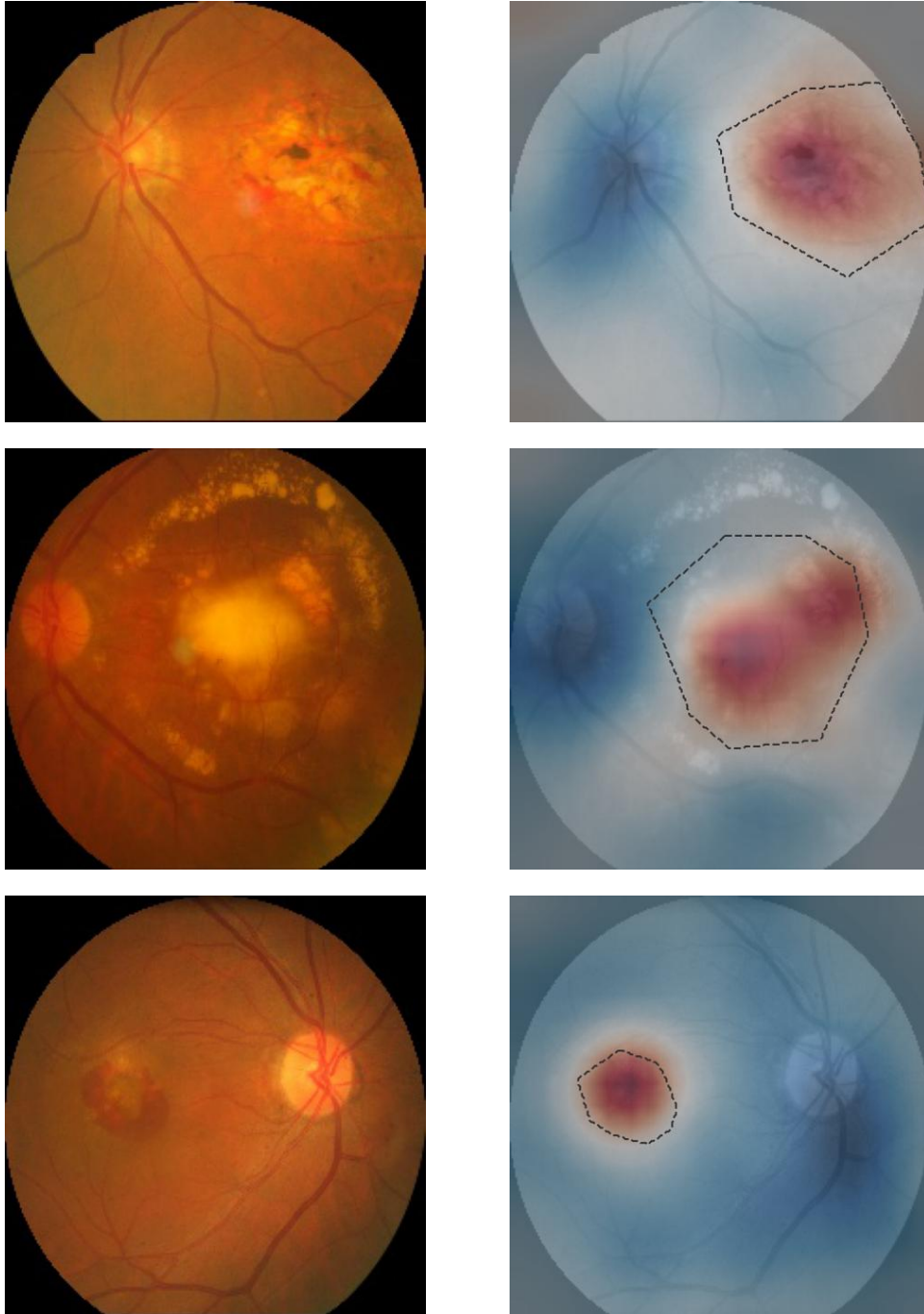
Extended Data Figure 3: Visualizations of pathology localization by AFLoc on retinal fundus photographs of **choroidal neovascularization**. Black dashed polygons indicate the pathology areas marked by eye doctors, and the intensity of red in the heatmaps signifies the focus level of the model's prediction, with deeper red indicating higher focus.